Investigation of a Dissipating Mesospheric Bore Using Airglow Imager and Direct Numerical Simulation

Kesava Ramachandran[1] [ID], **Mani Sivakandan[1]** [ID], **Jorge L. Chau[1]** [ID], **Juan M. Urco[1]** [ID], **Michael Gerding[1]** [ID], **Sven Grundmann[2]** [ID], and **Steven M. Smith[3]** [ID]

[1]Leibniz Institute of Atmospheric Physics (IAP) at the University of Rostock, Kühlungsborn, Germany, [2]Institute of Fluid Mechanics, University of Rostock, Rostock, Germany, [3]Center for Space Physics, Boston University, Boston, MA, USA

Abstract Atmospheric gravity waves play an important role in driving the dynamics of the Mesosphere and Lower Thermosphere and the basic structure of this region is determined by momentum deposition of these waves. Mesospheric bores are a type of non-linear response that cause the amplification of gravity wave, due to trapping, that is characterized by a propagating step-like jump followed by undulating waves. They require a stable layer or duct to travel horizontally with little attenuation thereby capable of transporting wave energy and momentum over larger distances. We present a prominent bright undular bore event observed in the mesospheric O(^{1}S), O$_2$, and OH emission layers on 16 March 2021 over Germany. A striking feature of this observation is the capture of bore's rapid dissipation around the center of the imager's field of view. The vertical temperature profile obtained from the satellite data indicates the presence of temperature inversion layer which acted as a thermal duct for the bore propagation. In addition, we have performed idealized two dimensional direct numerical simulations (DNS) of Navier-Stokes equations under Boussinesq approximation. The DNS results reproduce many important characteristics of the observed airglow event like the nonlinear wave-steepening, number of trailing waves, and its dissipation by implementing a thermal duct and a wave-like perturbation. Furthermore, the DNS results also indicate that the duct width and amplitude of the initial perturbation have a considerable effect on the bore morphology.

1. Introduction

The mesosphere and lower thermosphere (MLT) is the atmospheric region ranging between 60 and 120 km altitude that couples the lower and upper parts of the terrestrial atmosphere. The dynamic and composition changes in MLT region is primarily controlled by the solar and neutral atmospheric forcing from above and below, respectively. Moreover, part of the MLT is also a lower boundary of the Near Earth Space. Therefore, knowledge of its dynamics is of great importance in order to understand the behavior of the atmosphere as a whole in the growing space age. It has been well known that the dynamics of MLT region is mainly dominated by tides, and gravity waves which propagate upwards away from their tropospheric sources (Nappo, 2013). The waves that encounter the airglow layers typically have either band like or ripple-like structures (Peterson & Adams, 1983; Taylor & Hapgood, 1990). Although too faint to be detected by naked eye, these band-like structures occur rather frequently (Taylor et al., 1997) and can be measured by remote-sensing techniques such as airglow imagers. Multi-wavelength all-sky imaging of the nighttime mesospheric emission layers can provide valuable insights into structure and underlying dynamics of this region.

Taylor et al. (1995) reported one such "spectacular gravity wave event" in the mesosphere where the front of the wave had a marked brightness change relative to the background with wave crests and troughs in brightness appearing behind the front. Dewan and Picard (1998) first investigated this event and identified these structures as bores since their morphology resembled those of tidal bores (Lighthill, 1978). Bores have also been frequently observed in lower troposphere, one prominent example being the "Morning Glory" clouds in northern Australia (Clarke, 1972; R. K. Smith, 1988).

Mesospheric bores are non-linear responses that cause GW amplification, due to trapping (Fritts et al., 2020). Since the atmosphere is an open system this raises an interesting question: how do bounded ducts occur that can act as a wave-guide for the bores? According to the simple linear model put forth by Dewan and Picard (1998), based on the two-layer shallow-water theory of Rayleigh (1908), a ducting region caused by temperature inversion layer can act as a wave-guide that aids in bore propagation, similar to open channels in the case of tidal bores. Inside this duct the bore propagates in varicose mode, wherein the upper and the lower layers oscillate in-phase

or 180° out of phase with one another. Stable ducting regions in the form of either thermal ducts resulting from temperature inversion layer or from high wind shears where an altitude range is confined between regions of evanescence ($m^2 < 0$, m $= 2\pi/\lambda_z$ is the vertical wavenumber) (Chimonas & Hines, 1986; Isler et al., 1997) or a combination of both referred to as dual-ducting environment (Bageston et al., 2011; Chimonas & Hines, 1986) have been extensively reported in the literature. Since the theoretical explanation of mesospheric bores by Dewan and Picard (1998), numerous observations of bores in the mesosphere have been reported similar to the initial observation of Taylor et al. (1995) (Bageston et al., 2011; Fechine et al., 2005, 2009; Narayanan et al., 2009; Nielsen et al., 2006; She et al., 2004; S. M. Smith et al., 2003, 2005, 2017; Yue et al., 2010). Many of these observations were made using two or more airglow emission layers to provide evidence of sharp propagating fronts at different altitudes with large horizontal extension accompanied by trail of waves with increase (decrease) in brightness displacing the airglow emission layer below (above). In addition to airglow imaging observations, many studies employed simultaneous co-located temperature and/or wind measurements using lidars, radars and satellite to infer the background conditions during the propagation of bores (Brown et al., 2004; Fechine et al., 2009; S. M. Smith et al., 2003, 2005). Observations of standing wave structures resembling mesospheric fronts in noctilucent clouds (NLC) and undular bore-like structures in Polar Mesospheric clouds (PMC) have also been reported (Dalin et al., 2013; Dubietis et al., 2011; Fritts et al., 2020). A recent observation of Polar Meso-spheric Summer Echoes (PMSE) layer showed structures resembling a solitary wave propagating in varicose mode with extreme vertical velocities (∼50 m s^{-1}) (Chau et al., 2021). The new volumetric radar imaging used by Chau et al. (2021) to study this event with extreme vertical velocities and also other small-scale instabilities like Kelvin-Helmholtz Instability (KHI) in four dimensions (Chau et al., 2020) has greatly enhanced the study of small-scale dynamics relative to what has been possible by previous ground-based observations acting as a potential guide for the future modeling of small-scale dynamics.

While the occurrence of mesospheric inversion layers (MIL) is quite frequent, that of bores is not. Studies using airglow emissions and satellite observations of mesospheric bores suggest that the possible sources for the bores could originate from quasi-monochromatic GWs, mesospheric fronts to diurnal tides in the equatorial latitudes and semi-diurnal tides in the midlatitudes (Bageston et al., 2011; Hecht et al., 2001; Hozumi et al., 2018, 2019; Narayanan et al., 2009; S. M. Smith et al., 2003; Taylor et al., 1995; Walterscheid et al., 1999). Dewan and Picard (2001) suggested that the critical level interaction of GWs with the background mean flow could also be a potential forcing mechanism for the bore generation. Previous studies by S. M. Smith et al. (2003, 2017), and Yue et al. (2010) associated the generation of mesospheric bores with a tropospheric cold front generated GWs. The statistical analysis carried out by Hozumi et al. (2019) using 3 years (2012–2015) of data from Visible and near Infrared Spectral Imager (VISI) onboard the International Space Station (ISS) reported the latitudinal dependence of the mesospheric bores. They showed the occurrence of mesospheric bores is high during equinox at equatorial latitudes and winter at mid-latitudes. They also suggested that the high probability of MILs caused by atmospheric tides and GWs at these latitudes could be a reason for the latitudinal dependency of bore occurrence. More recent modeling and theoretical studies of mesospheric bores in thermal and Doppler ducts were carried out by Seyler (2005) and Laughman et al. (2009) where they solved the Navier-Stokes (NS) equations of a stratified fluid describing incompressible non-linear dynamics. Their results confirmed some of the earlier results of bores like the amplitude steepening of a long wavelength GW evolving into a bore, the separation of the peaks and the amplitude dependant phase speed (Lighthill, 1978; Seyler, 2005).

In this paper, we report and discuss a bright wave event that was observed by an all-sky imager propagating from Southwest to Northeast direction between 90 and 97 km on 16 March 2021 over northern Germany. Morphologically this event resembled an undular bore due to the presence of a sharp wavefront followed by trailing waves. An interesting aspect of this event was its rapid dissipation which was captured within the field of view (FOV) of the imager. To complement the observations, we have performed two-dimensional (2D) direct numerical simulations (DNS) of idealized Navier-Stokes equations under Boussinesq approximation. In doing so, we have reproduced many of the essential bore parameters like the generation of trailing waves from an initial disturbance in a thermal duct, separation of crests as the bore evolves, the time taken for the bore to dissipate. Compared to the study of (Seyler (2005)), our simulations employed an initial perturbation which is only a small fraction of the entire horizontal domain. Furthermore, the responses to different initial perturbations and ducting environments were also investigated.

The paper is structured as follows: Section 2 explains the methodology undertaken in the paper which includes an overview of the instruments used: (a) Airglow imager, (b) TIMED SABER, and (c) SIMONe radar network. The Navier-Stokes equations under Boussineq approximation are derived and the simulation setup along with the

initial conditions are described in detail in this section. In Section 3 the results of airglow observations and the DNS are presented. In Section 4 the observation and simulation results are compared and interpreted. Section 5 summarizes and concludes the paper.

2. Methodology

2.1. Observations

2.1.1. Airglow

The multi-wavelength all-sky imager (ASI) installed by Boston University and operated at the Leibniz Institute of Atmospheric Physics (IAP) in Kühlungsborn (54.12°N; 11.77°E) is equipped with six interference filters enabling the observation of different altitudes of the MLT and ionosphere. The imager has $1,024 \times 1,024$ charge coupled device with 13 μm pixels and anti-reflection coating and modern electronics. The front optics of the imager consists of a 16 mm fish-eye lens with a maximum field of view (FOV) of 180°. The present study uses two narrow band filters to observe night-glow emissions in the MLT at wavelengths of 557.7 nm ($O(^1S)$ green line) and 864.5 nm (O_2 emission), and a broadband OH emission filter with a spectral range of 695–1,050 nm. The 557.7 nm and the 864.5 nm emissions are caused by the excitation of atomic $O(^1S)$ and molecular oxygen O_2, having a peak emission altitude of 97 and ∼93 km respectively, while the OH emission is caused by the chemical reaction of hydrogen and ozone with a peak altitude of 87 km. It is to be noted here that the peak emission altitude of OH emission was at ∼90 km on 16 March 2021. The emission altitude of the airglow layers were obtained from SABER TIMED satellite measurement on 16 March 2021 at around 23:58 UT, right at the end of the wave event (see Figure S1 in Supporting Information S1). The integration time for each filter and the duty cycle for the full set of operations can be adjusted for either routine data-taking or campaign-mode observations (Martinis et al., 2018). In the present case, only four filters were operational with the exposure time of 110 s for $O(^1S)$ and $O(^1D)$, 60 s for O_2, and 15 s for the broadband OH filter. The duty cycle is ∼5 min. On this night, the observation was started at 18:30 UT and continued till 04:30 UT, during this span of time each filter provided nearly 140 images. Airglow emissions have been used for many years as a tracer to study atmospheric wave dynamics by measuring the changes in the intensity of the emissions as a consequence of wave propagation. Moreover airglow imaging technique is widely used to directly estimate wave characteristics like the wavelength, phase speed, periodicity and propagation direction. Before extracting the wave information, the raw images were processed following the standard methods of image processing including geospatial calibration, star removal, and unwarping (Garcia et al., 2000; Sarkhel et al., 2022; Sivakandan et al., 2019). To further enhance the visual contrast of airglow intensity perturbation in the chosen images, we first calculated the percentage difference image/residual image (Ip). Residual images are created by picking a central image (I) and averaging it with other images taken 30 min before and after. The resulting average (Ira) is therefore an hourly running average centered on image, I. From this, the hourly average is subtracted from the central image and normalized with the hourly average to obtain the residuals (Ip = ((I–Ira)/Ira) × 100). The residual images are shown in Figure 2 (However, in Movie S1, raw images were used as it is). The bore parameters were derived from image analyses. When examining an image, the distance between the successive peaks or troughs is considered to be one wavelength. The temporal evolution of the positions of these phase fronts from a given image to the successive image provides phase velocity. A detailed description of this method is available in Sivakandan et al. (2019).

2.1.2. TIMED SABER Data

Temperature profiles obtained from the Sounding of the Atmosphere using Broadband Emission Radiometry (SABER) onboard Thermosphere Ionosphere Mesosphere Energetics and Dynamics (TIMED) satellite were used as supporting information to characterize the background thermal structure on the day of the event. The ambient kinetic temperature retrieval at particular altitude is accomplished using the 15 μm emission from CO_2 molecules in the atmosphere assuming the local and non-local thermodynamic equilibrium condition. The uncertainty in retrieved SABER temperature in the MLT region is around 4–5 K with a vertical resolution of 2 km (García-Comas et al., 2008). There were two temperature profiles available, at 23:58 UT and 23:59 UT, approximately 400 kms from the center of bore observation location on the day of the event. Due to the yaw cycle of SABER during this time, no data north of 52°N is available.

2.1.3. SIMONe Winds

In MLT, ducts can also be sustained through a layer of wind gradient. MLT winds were obtained with a multi-static specular meteor radar network in northern Germany with a SIMONe (Spread-spectrum Interferometric Multistatic meteor radar Observing Network) implementation (Chau et al., 2019). During this period, the system consisted of three transmitters located in Kühlungsborn (54.12°N, 11.77°E), Collm (51.31°N, 13.00°E), and Juliusruh (54.63°N, 13.37°E). Kühlungsborn and Collm operated coded-CW and pulsed sequences, respectively. On reception, Neustrelitz (53.33°N, 13.07°E), and Bornim (52.44°N, 13.02°E) sites consist of five receivers each, that are able to receive all three transmitter signals, while the other single-receiver sites receive only Kühlungsborn before July 2021, and Juliusruh-Kühlungsborn afterward. In summary, there have been two receiver stations with Multiple-Input Multiple Output (MIMO), five(four) receivers with Single-Input Multiple-Output (SIMO), and one(two) receiver(receivers) with Multiple-Input Single Output (MISO) before(after) July 2021. These configurations make a total of 9(11) multistatic links before(after) July 2021. More single-receivers are being added to the network, currently with 19 multistatic links. Measurements from multistatic links aim to provide more reliable information about mesoscale dynamics by observing more meteors from different viewing angles (Asokan et al., 2022; Conte et al., 2022; Poblet et al., 2022). For details about MIMO, SIMO and MISO techniques we refer the reader to Chau et al. (2019).

2.2. Direct Numerical Simulations

While a plethora of literature exists predominantly on the observation of mesopsheric bores by different ground and space based measuring techniques, the same does not hold true regarding numerical simulations of these events. Many important questions still remain open concerning the mechanisms of generation of mesospheric bores (Fritts et al., 2020; S. M. Smith et al., 2003). To complement our observations we also ran DNS of incompressible Navier-Stokes equations based on Bousinessq approximation where the density differences are considered negligible except in the buoyancy term (Nappo, 2013; Seyler, 2005). The framework used for running the simulations is called Dedalus which solves the differential equations using pseudo-spectral methods. Dedalus is designed to solve initial-value, boundary-value, and eigenvalue problems involving nearly arbitrary equations sets (Burns et al., 2020).

The incompressible Navier-Stokes equations of a stratified fluid are as follows,

$$\partial_t \mathbf{u} + \mathbf{u} \cdot \nabla \mathbf{u} = -\frac{\nabla p}{\rho} - \mathbf{z}g + \nu \Delta \mathbf{u} \tag{1}$$

$$\partial_t \theta + \mathbf{u} \cdot \nabla \theta = \kappa \Delta \theta \tag{2}$$

$$\nabla \cdot \mathbf{u} = 0 \tag{3}$$

Here $\mathbf{u} = (u,w)$ are the horizontal and the vertical components of the velocity respectively, p is pressure, ρ is the mass density, θ is the potential temperature, ν is the kinematic viscosity and κ is the thermal diffusivity. The simulations done by Seyler (2005) did not consider the effect of dissipation when using potential temperature as a passive scalar on the bore evolution whereas this term is included in our equations (see Equation 2).

The divergence free condition allows us to write the above equations in streamfunction-vorticity formulation with the streamfunction(ψ) given by,

$$\mathbf{u} = -\mathbf{j} \times \nabla \psi, \quad u = -\frac{\partial \psi}{\partial z}, \quad w = \frac{\partial \psi}{\partial x} \tag{4}$$

The streamfunction and vorticity are related by

$$\zeta = -\left(\partial_x^2 + \partial_z^2\right)\psi \tag{5}$$

where ζ is the y component of vorticity.

Taking the y component of the curl of Equation 1 and assuming Boussinesq approximation by writing the density and pressure as $\rho = \rho_0 + \rho'$, $p = \tilde{p} + p'$ and making use of hydrostatic pressure balance ($d\overline{p}/dz = -\rho_0 g$, ρ_0 is the basic state density), we get the following relations,

$$\partial_t \nabla^2 \psi + [\psi, \nabla^2 \psi] = -\partial_x \theta + \nu \Delta \psi \tag{6}$$

$$\partial_t \theta + [\psi, \theta] = N^2(z)\partial_x \psi + \kappa \Delta \theta \tag{7}$$

The potential temperature is written in terms of its equilibrium state and perturbation, $\theta = \bar{\theta}(z) + \theta'$. The buoyancy frequency is then given by

$$N^2(z) = -\frac{g}{\theta}\frac{d\bar{\theta}}{dz} \tag{8}$$

and $[A, B] = \partial_x A \partial_z B - \partial_z A \partial_x B$ is the Jacobian. μ is the kinematic viscosity.

For further details on the equations derived here, the reader is referred to Nappo (2013) and Seyler (2005). All the simulations presented in this study assumed 2-D non-linear dynamics and a domain having periodic horizontal boundary conditions (Fourier coordinates) and rigid upper and lower boundaries (Chebyshev coordinates) (Burns et al., 2020). The upper and lower boundaries are defined by no-slip boundary conditions. The simulation domain employed a grid of 1,024 spectral modes in the horizontal and 256 modes in the vertical. It is well known that for the generation of undular bores some form of ducting structure needs to be present (thermal or Doppler) to act as a guiding channel for their evolution and propagation (Dewan & Picard, 1998; S. M. Smith et al., 2003). This ducting structure in the simulations is given in the form of an idealized stability profile (N^2) from which the background temperature profile can be obtained using Equation 8. Following Seyler (2005), we let the buoyancy period at the maximum of the stability duct to be our fundamental time scale (N^{-1}) and the half width of duct to be the length scale. The values for the maximum value of the stability profile and the half-width of the duct in the simulations are taken from the observation data ($N^2 = 1 \times 10^{-3} s^{-2}$ and 1.5 km). The corresponding kinematic viscosity in the mesopause altitudes is around 10 m^2 s^{-1} (Hines, 1960) and when non-dimensionalized with respect to the length and time scale yields a value of 0.001 (Seyler, 2005). We set $\nu = \kappa$ so that Prandtl number is 1. This value of kinematic viscosity is large enough to have an effect on the bore formation. The simulations are initialized with a sinusoidal waveform imposing the streamfunction and potential temperature perturbations. Since the vertical domain is bounded, the vertical wavelength is chosen to be comparable to the thickness of the duct in each case. The initial streamfunction and potential temperature (non-dimensional) perturbations are of the form,

$$\psi(x, z, 0) = A \sin\left(\frac{2\pi\left(x - \frac{L_x}{2}\right)}{L_x}\right) \sin\left(\frac{n\pi z}{L_z}\right) * G(x) \tag{9}$$

$$\theta(x, z, 0) = -\frac{0.4\pi A}{L_z} A \sin\left(\frac{2\pi\left(x - \frac{L_x}{2}\right)}{L_x}\right) \sin\left(\frac{n\pi z}{L_z}\right) * G(x) \tag{10}$$

$$G(x) = \exp\left(-\frac{(x - L_x/2)^2}{L_x}\right) \tag{11}$$

where A is the non-dimensional amplitude of the initial perturbation, L_x and L_z are the non-dimensional horizontal and vertical wavelengths, respectively. These values are non-dimensionalized with respect to the chosen length scale. The initial perturbations of the streamfunction and the potential temperature are multiplied by a Gaussian envelope function $G(x)$, given by Equation 11, so that the initial perturbation is centered in the domain. In doing so, the initial perturbation becomes only a fraction of the horizontal extent of the simulated domain. This is in contrast to the approach employed by Seyler (2005) where the given initial perturbation was a long wavelength ducted GW over the entire horizontal domain. All the simulations in this paper have non-dimensional vertical and horizontal wavelengths of 3 and 60, respectively. The size of the horizontal and the vertical domain are 200 and 3.0 (non-dimensional values), respectively. The stability profile with which the model was initialized is given by the expression $N^2(z) = 0.2^2 + \exp\left(-(z/\sigma)^4\right)$, where σ describes the width of the duct (Laughman et al., 2009; Seyler, 2005). In Seyler (2005) only a constant ducting environment was studied, in our study the width of the ducting layer was varied to see its effect on bore evolution. Figure 1b shows some of the different background
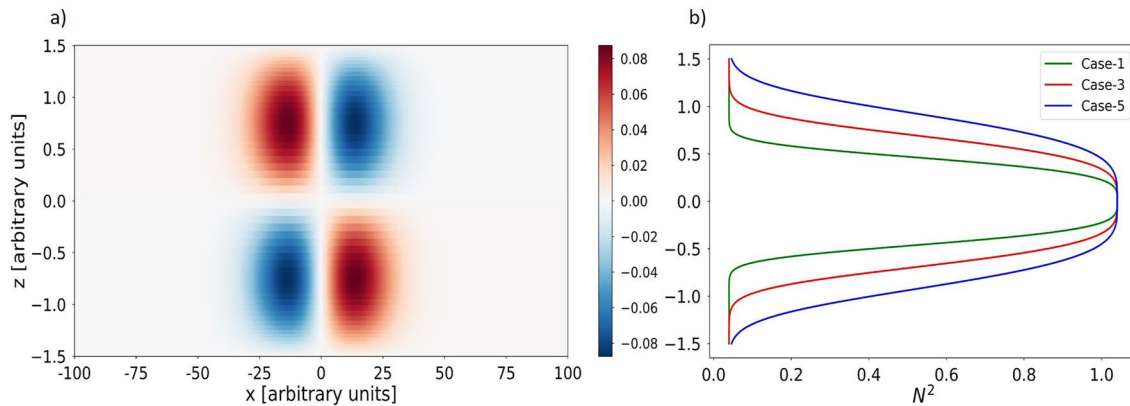
Figure 1. (a) xz cut of the simulation domain. The color contours represent the non-dimensional initial perturbation of potential temperature signifying ducted gravity waves. Notice that the initial perturbation does not span the entire horizontal domain. (b) Background ducting environments (N^2) considered in the DNS. Case-1 (green) has a non-dimensional FWHM value of ~1, Case-3 (red) has FWHM ~ 1.5, Case-5 (blue) has FWHM ~ 2

thermal ducting environments considered in the simulations. Case-1 (green line) implies a stability profile with non-dimensional Full Width at Half Maximum (FWHM) value of ~1 (narrow duct), Case-3 (red line) a FWHM value of ~1.5, Case-5 (blue line) a value ~2 (wide duct). Other ducting conditions that were considered are FWHM ~ 1.25 (Case-2) and 1.75 (Case-4), respectively.
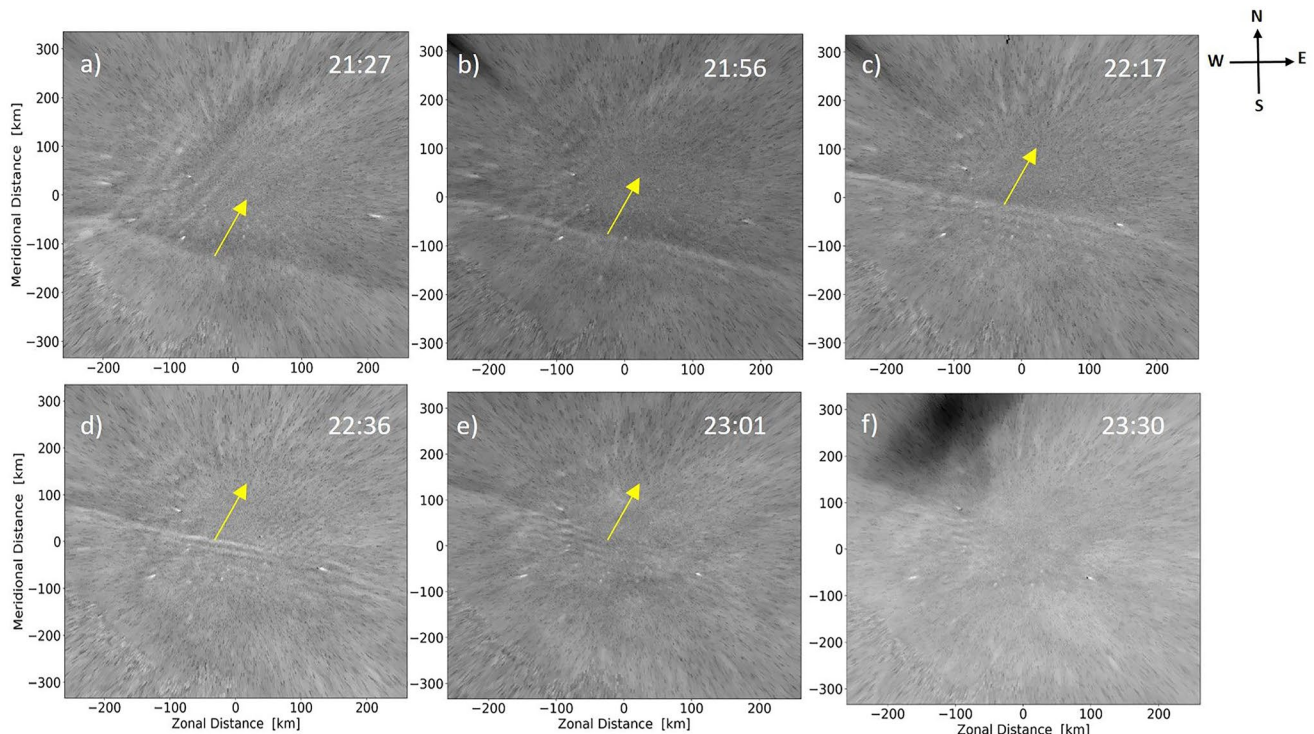

Figure 2. A sequence of O(^{1}S) 557.7 nm airglow images on 16 March 2021 over northern Germany. A front-like structure appeared in the south-western edge of the image at around 21:30 UT and propagated northeast in the consecutive images followed by trailing waves. The yellow arrow points in the direction of propagation.

3. Results

3.1. Observations

A series of images showing the bright mesospheric front observed in $O(^1S)$ airglow emission layer are presented in Figure 2, on the night of 16 March 2021 over northern Germany between 21:30 and 23:30 UT (Universal Time). This sequence of images shows the evolution, propagation and the dissipation of the bore. At time 21:27 UT we observe a lone wave front entering the FOV of the imager from the southwest direction. Initially, left side (western side) of the wavefront is more clearly visible than the right side (eastern side) due to the predominant cloud activity which had masked half of the horizontal extent of the wavefront. One can also see a slight "bend" of the wavefront (see Movie S1) along the zonal direction at 21:27 UT which is not seen at later times as the front propagates. Although the cause of this "bend" is not immediately known, it could be a small horizontal undulation of the wavefront (Hozumi et al., 2018; Mondal et al., 2021). The full wavefront is visible from 21:50 UT with an elongation in the East-West(EW) direction. A this time we also see the appearance of trailing waves behind the leading wavefront. Over the next 30 min more trailing waves start to appear as the front propagates and they are phase locked to leading front. This feature of a leading edge wavefront with the trailing waves fits the description of an undular mesospheric bore (Dewan & Picard, 1998) rather than a "wall" event which must exhibit both a leading and a ending edge (Brown et al., 2004; Li et al., 2007). At time 22:36 UT the trailing waves span the entire horizontal extent of the FOV of the imager, at least 400 km with a reduction in their horizontal extent at later times. A maximum of three trailing waves are observed when the bore reaches the zenith between 22:20 and 22:36 UT before the bore dissipates into the background. The dissipation first starts on the right side of the image as one can still see the frontal structure on the left side of the image at 23:00 UT. The dissipation then takes over the entire bore with the time for dissipation being less than 25 min.

Also seen at 21:27 UT are gravity waves propagating toward northwest and disappearing from the FOV of the imager at around 22:00 UT. These waves span almost the entire meridional distance of at least 400 km with wavelengths in the range of 18–60 km. From our analysis of the observation, we believe that this large-scale gravity wave could not have had any role in the formation of the bore because, (a) its propagation direction is perpendicular to the bore propagation direction, (b) It does not dissipate within the FOV so it could not have contributed to the formation of the thermal duct. However, we cannot deny that it may have had some effect on the propagation of the bore but with available data set we cannot evidently show what effects these large scale GW could have had on the bore itself. Therefore, it is not considered for further discussion in this paper.

This bore event was also observed in the O_2 and the OH layers, with the peak emissions on this night at altitudes near 93 and 90 km, respectively (see Figures S2 and S3 in Supporting Information S1). The leading wavefront is visible however, the apparent presence of trailing waves as seen in the $O(^1S)$layer cannot be clearly identified in these two layers. The short "bend" which was seen in the $O(^1S)$ layer is clearly visible in O_2 layer where it resembles the shape of a bow. This further indicates that the wavefront indeed exhibits a very small horizontal undulation and therefore is an observed feature and not an artifact of instrumentation or analysis. The GWs which were seen propagating in the Northwest direction are also apparent in O_2 layer. As in the $O(^1S)$ layer, the bore reaches the zenith of the imager after which it starts to dissipate with the eastern side dissipating faster than the western side. Interestingly, the presence of small scale ripple-like structures were noted in the center and eastern side of the images between 22:30 UT and 22:50 UT (Peterson & Adams, 1983; Taylor & Hapgood, 1990). Since this undular bore event was observed in $O(^1S)$, O_2 and the OH airglow emission layers, we can say that the height of the bore is at least 7 km.

In order to investigate the vertical propagation characteristics of the wave structures if any, the intensity of $O(^1S)$, O_2, and OH layers were plotted by rotating the residual images by an azimuth angle of 14° in the anti-clockwise direction from North and then taking an average in the direction perpendicular to the bore propagation. The observed phase speed calculated from $O(^1S)$, O_2, and OH images are 30 ± 7 m/s, 25 ± 6 m/s, and 28 ± 5 m/s, respectively. Due to the instrumental setup, the filters cannot provide simultaneous observations of all three layers, thus there will be a small time delay between each measurement. In the present case, time delay (dt) between $O(^1S)$, O_2, and $O(^1S)$, OH are 61 and 88 s, respectively. In order to see the simultaneous intensity variation, we have estimated the horizontal displacement (d = dv/dt, v is mean speed of the bore i.e., ~27.5 m/s) of the bore during the above mentioned time delays. Finally, these displacements are added with O_2 and OH distance scale (x-axis). To put it in a more concise manner these intensity curves have been horizontally shifted based on the calculated phase speed of the leading front and taking average phase speed of three layers as a reference to
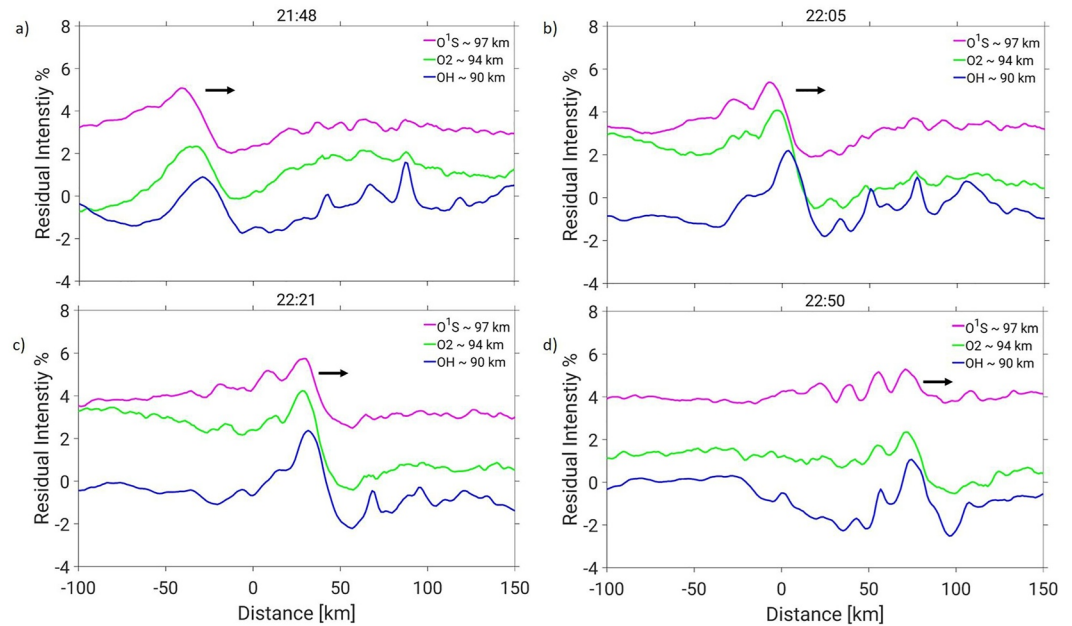
Figure 3. (a–d) The magenta, green and blue solid lines in each panel depict the intensity variation of O(^{1}S), O$_2$ and OH airglow emissions at constant time, respectively along their line of propagation. The black arrow indicates the propagation direction.

account for the time difference between each image in the different layer as shown in Figure 3. Figure 3 shows the intensity variation of O(^{1}S), O$_2$, and OH layers as magenta, green and blue lines, respectively in different layers at the same time in each frame. The phase propagation plot at time 21:48 UT indicates a clear lag between the different layers with a downward phase progression which clearly indicates an upward propagating gravity wave that may have been the cause of the observed bore. Within 17 min (at 22:05 UT) the phase lag is almost negligible in the O(^{1}S) and O2 images however there is still a small lag in the OH layer. This suggest that the upward propagating GWs may have been trapped in a duct region around the O(^{1}S) emission altitude and evolved as a bore. Around 22:21 UT, the perturbations are in-phase in all the three layers and the presence of trailing wave undulations are evident here. The increase in the brightness intensity following a step-like jump is consistent with the complementary effects of airglow layers proposed by Dewan and Picard (1998) wherein here the passage of the bore pushes the layer downwards to a warmer region and the layers become denser and brighter. Therefore we can conclusively say that the observed event is an undular mesospheric bore since the relative changes in the airglow emissions are in-phase with one another. This is in contrast to the "wall" wave theory where an upward propagating GW, with a clear leading and ending edge, leads to a significant time delay between different airglow emission layers which results in the layers neither being in-phase nor out of phase (Li et al., 2007).

The altitude profiles of the background temperature and the static stability (N^2) at two different locations situated within ~400 km from the center of the bore observation location are shown in Figure 4. In this figure different airglow emission layers are marked by horizontal dotted lines. The level-2 temperature data from SABER is available for 300 m resolution in the vertical which was then interpolated for to 1 km in order make the vertical resolution consistent with the winds measured from the SIMONe system. One can discern the presence of two inversion layers in SABER-1 profile: an upper and a lower inversion layer of magnitudes ~15 and ~20 K between the altitudes 95–97 km and 88–90 km, respectively while in SABER-2 there is a MIL of magnitude ~15 K only between the altitudes 95–97 km. Since all the three airglow emission layers show a bright bore, it is reasonable to assume that the bore is located near the highest emission altitude that is, O(^{1}S) layer. SABER v2.0 satellite measures energy emitted from a volume with a horizontal smearing of 200–300 km (Dawkins et al., 2018) and the measured temperature profile should be taken as a representative background profile of the whole region scanned by the instrument. It should be noted here that the available temperature profiles were measured by SABER at 23:58 UT and 23:59 UT, just 20 min after the event. Due to this, even though it may seem that the dissipation of the bore could have contaminated the MIL, it should be kept in mind that the location of the event was ~400 km
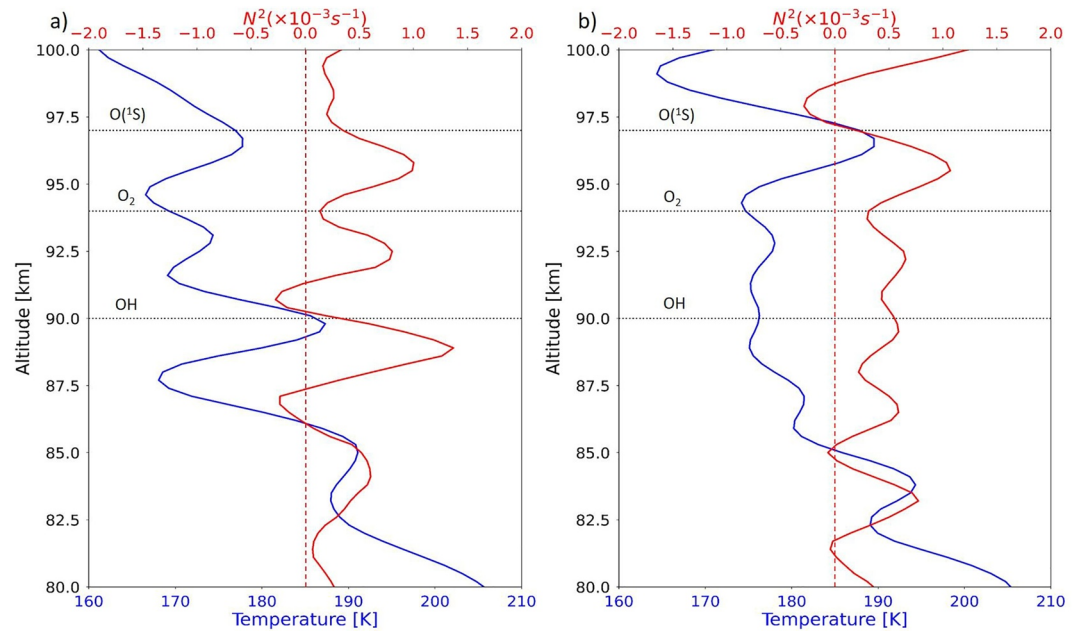
Figure 4. (a) SABER-1 (23:58 UT, 50.10°N, 9.57°E) and (b) SABER-2 (23:59 UT, 51.06°N, 15.47°E) represents the vertical profile of temperature from SABER (blue line) and the corresponding squared Brunt-Väisälä frequency (N^2) profile (red line) at two different locations on 16 March 2021. The horizontal solid lines indicate the peak emission altitudes of O(^{1}S), O$_2$, and OH airglow emissions on 16 March 2021. The vertical red dashed lines point to zero value in the stability profile. A persistent inversion layer is visible between 95 and 97 km.

away from where the temperature measurement was made. So we can say with a good degree of certainty that the measured temperature profile can be taken to represent the background temperature condition. Moreover, the vertical profile of N^2 also displays a weak duct region near the O(^{1}S) peak emission (altitude) at both the locations. Therefore, we assume that this duct supported the formation of the bore around the O(^{1}S) (altitude).

We also looked into the wind variations for two consecutive nights using the SIMONe winds over northern Germany which can give a comprehensive outlook into the background dynamics of the observed bore. Figure 5 shows the hourly averaged zonal and meridional wind components on 15 and 16 March 2021. The vertical dashed lines indicates the time duration of the observed mesospheric undular bore. On the day of the bore event, that is 16 March 2021, we see a clear pattern that resembles semi-diurnal tide activity both in the zonal and meridional winds. Additionally, the magnitudes of the zonal and meridional winds were at least 20–30 m/s larger than on the previous day right before the onset of the bore. Moreover, near the O(^{1}S) layer both zonal and meridional winds display a change in direction from east to west and north to south before and during the bore event, respectively. This suggests that in addition to the thermal duct provided by the temperature inversion, the wind gradient may also have had some contribution in the form of Doppler duct to the formation and propagation of the bore on this night. The resultant wind has mostly eastward at 90 km, it changed to southward at 94 km. Coincidentally, the resultant wind was in the southwest direction at 97 km which is the level of peak O(^{1}S) emission, which nearly is opposite to the direction of bore propagation.

With the available temperature and wind profiles, one can use the Taylor-Goldstein equation to characterize the environment of gravity wave propagation,

$$m^2(z) = \frac{N^2}{(c-u)^2} + \frac{U_{zz}}{(c-u)} - k^2 - \frac{1}{4H^2} \tag{12}$$

Here N is the Brunt-Vaisala frequency, u is the mean wind in the direction of the wave propagation, c is the observed horizontal wave phase speed, U_{zz} is the curvature of the wind flow, H is the scale height, and k and m are the horizontal and vertical wavenumbers, respectively. Figure 5c shows the calculated vertical wave number (m^2) as a function of height for the O(^{1}S) emission layer right before the onset of the event at 21:30 UT on 16 March 2021. It is clear from this figure that there is a region near 97 km altitude where GW propagation is allowed ($m^2 > 0$) which is bounded
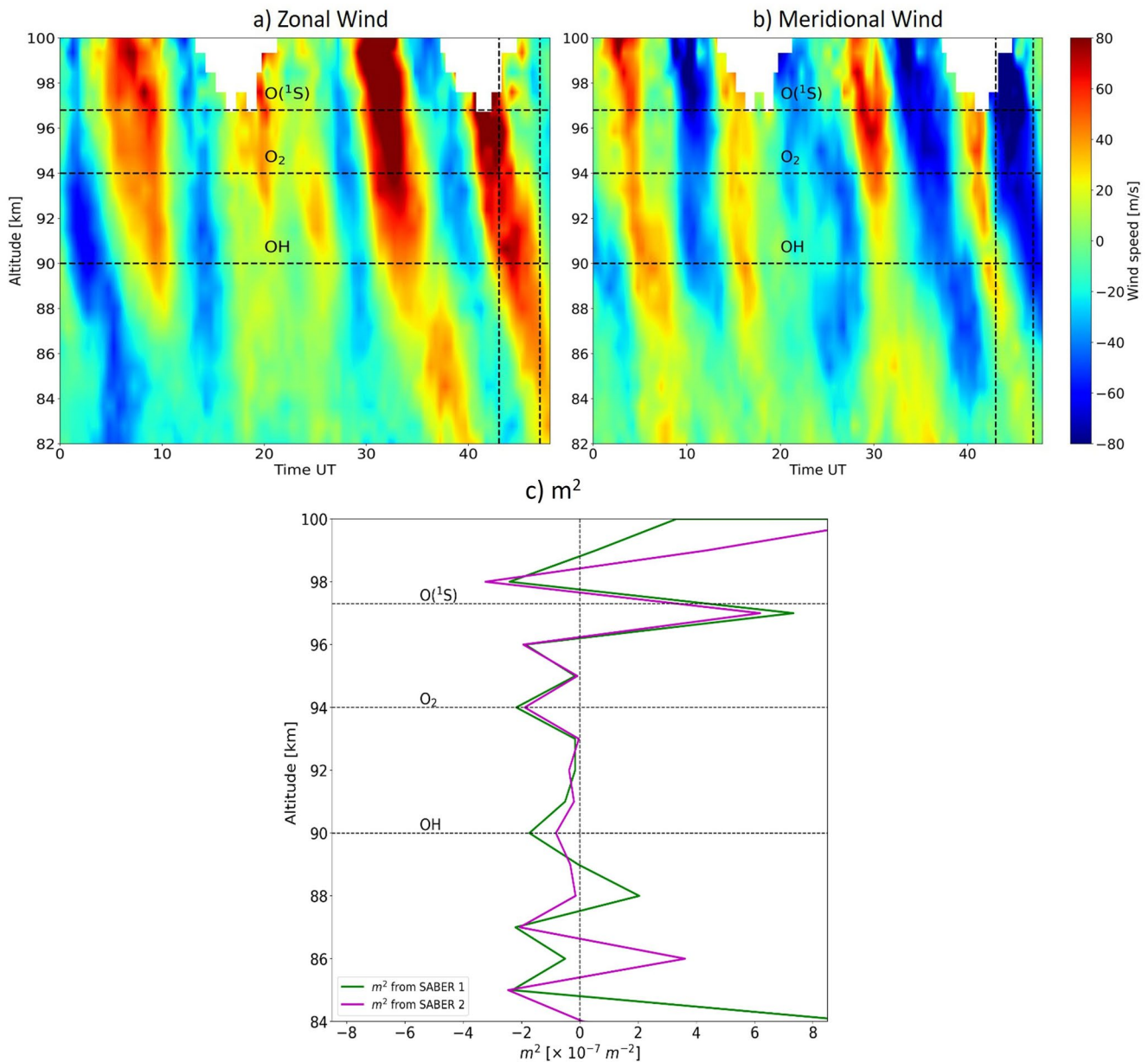
Figure 5. (a) The zonal, (b) the meridional winds on 15 and 16 March 2021. The horizontal dotted lines indicate the peak emission altitudes of $O(^1S)$, O_2, and OH airglow emissions on 16 March 2021. The two vertical dotted line indicate the time limit of the bore event on 16 March 2021. (c) Profiles of m^2 derived from SABER 1 (green line), SABER 2 (magenta line) and the winds.

by regions of evanescence ($m^2 < 0$) at 96 and 98 km. This profile along with the temperature and stability profile supports our assumption that the duct that enabled the bore propagation was centered near the $O(^1S)$ emission altitude.

A brief overview of the results from the observation is as follows:

- A mesospheric bore event was observed in $O(^1S)$ airglow emission layers whose dissipation occurred within the FOV of the imager. We classify this as an undular mesospheric bore due to the presence of ~3 trailing undulations which follows the leading wavefront. The wavelength of the leading wavefront was ~25 km. The bore dissipated rapidly while entering the zenith of the imager FOV in a period of less than 25 min.
- According to the complementary effects proposed by Dewan and Picard (1998), we classify this bore as a bright bore in all the three airglow emission layers. The temperature profile obtained from SABER indicates the presence of temperature inversion layer near the $O(^1S)$ airglow emission altitude
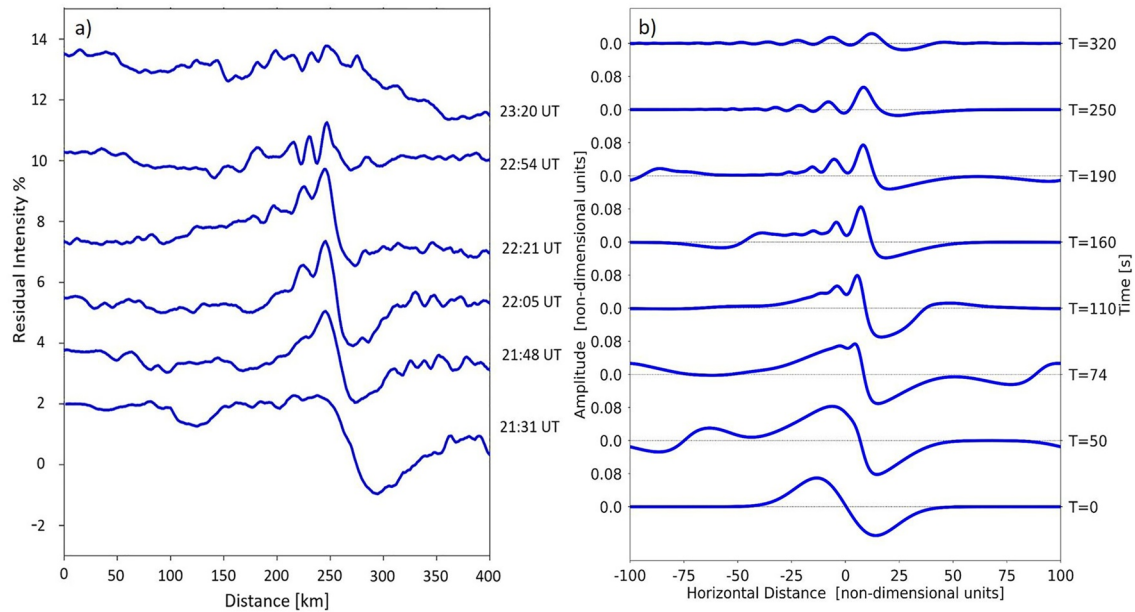
Figure 6. (a) Brightness intensity plot showing the temporal and spatial evolution of undular bore in O(^{1}S) 557.7 nm airglow emission. The lines are shifted vertically by an offset factor of 2 to represent the time evolution. The time series was obtained by rotating the residual images by an azimuth angle of 14° in the anti-clockwise direction from North and then taking a zonal average (i.e.,) in the direction perpendicular to the bore propagation. (b) Potential temperature traces from DNS representing the undular bore evolution with initial amplitude, $A \sim 0.08$ for Case-5 (FWHM 2) with constant background wind.

- The zonal and meridional winds indicate a semi-diurnal tidal activity before the onset of the bore. The resultant wind is nearly in the direction required for the bore propagation. The resulting wind gradient may also have had some contribution in the form of Doppler duct to the formation and propagation of the bore.

3.2. Direct Numerical Simulations

We complemented our observational results by running a series of direct numerical simulations subjected to a variety of initial and background conditions. Figure 6 show the evolution of undular bore structure in O(^{1}S) layer (left side) and DNS (right side). The brightness intensity of O(^{1}S) layer in Figure 6a shows the phase-aligned morphology of the bore at different times. The time series was obtained by rotating the residual images by an azimuth angle of 14° in the anti-clockwise from North and then taking a zonal average (i.e.,) in the direction perpendicular to the bore propagation. Each brightness trace has been offset by a constant factor of 2 in the vertical for clarity with the lowest trace corresponding to time 21:30 UT and the top trace to time 23:20 UT. At 21:30 UT, we see that there is a decrease and a subsequent increase in the brightness intensity at approximately 250–300 km. When an airglow layer is pushed down adiabatically, it becomes warmer, denser and presumably results in an increase in the brightness intensity (Dewan & Picard, 1998). At 21:48 UT, we see the appearance of a sharp peak and of the first trailing wave at 22:05 UT. A couple of more trailing wave undulations start to form as the bore propagates. At around 23:15 UT there is hardly any signature of the wavefront being present leading us to conclude that the dissipation of the bore had taken place.

In Figure 6b is shown the time evolution of bore from DNS with the background thermal duct having non-dimensional FWHM value of 2, initial amplitude of perturbation, $A \sim 0.08$ and a constant background wind with a non-dimensionalized value of 1. It is known that wind shear plays an important role in the formation of the duct (Fechine et al., 2009; Laughman et al., 2009; S. M. Smith et al., 2017) but the main focus of the present study is to evaluate to what extent the thermal duct alone could explain features of the observed bore. The line traces have been shifted horizontally by removing the bore's velocity and are depicted in the frame of reference where the bore is stationary. The lowest trace corresponds to time $T = 0$ s with each subsequent trace offset by a constant value for clarity representing the time evolution (notice the time axis on the right side of the figure). As we can see, at time $T = 0$ s, the 2D system is initialized with a sinusoidal waveform perturbation which is most efficient in forming bores (Seyler, 2005). At time $T = 50$ s we see that the initial wave experiences a non-linear
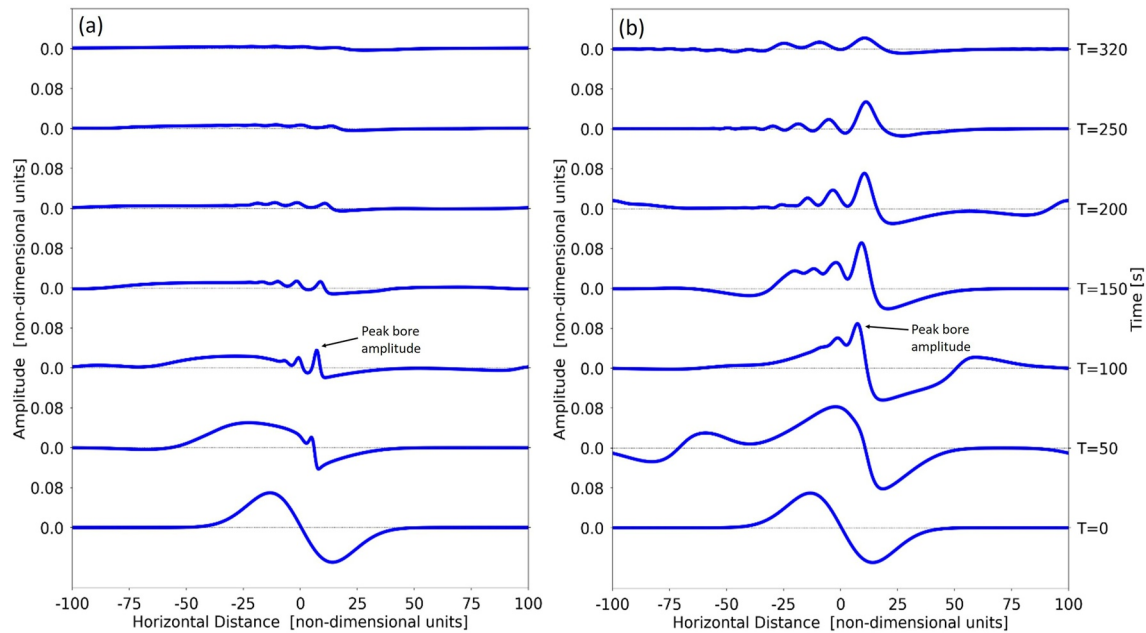
Figure 7. (a) Potential temperature traces for Case-1 (FWHM of stability profile ~1) with initial amplitude, $A \sim 0.08$ (b) The same for Case-5 (FWHM of stability profile ~2). The inset text shows the peak amplitude value of the bore. Each trace has a constant offset added to it to refer the time evolution. Refer to the text for more details.

steepening which resembles the wave steepening observed in the O(^{1}S) layer at 21:30 UT (Figure 6a). At later times, $T = 100$ s, 150 s, 200 s, we see the evolution of the wavefront from the non-linear steepening to a sharp peak and the ensuing trailing wave undulations that start to form as the front starts to lose its amplitude. A total of 3 trailing waves were simulated in this case.

The non-linear response of the bore reported here is similar to that of Seyler (2005) with a major quantitative difference in that, here the non-linear evolution of the bore has resulted from an initial perturbation which is a fraction of the horizontal domain simulated. It has been noted previously that the bore loses energy in two ways, either the wave energy is partitioned out from the duct or in the form of more trailing waves (Dewan & Picard, 1998; S. M. Smith et al., 2003). This can be seen in Figure 6 where the amplitude of the bore front decreases as more trailing waves are added. Also to note from the simulations is the increase in the separation between the successive wave crests (peaks) as the bore evolves which agrees with the results of Seyler (2005) whose results also indicated that the separation between the peaks increased with time. The analytical model of Dewan and Picard (1998) assumes that the separation between the successive crests is constant.

Encouraged by the qualitative agreement of simulations and observations, we carried out numerical studies to explore the effects of different initial perturbations and duct widths on the bore evolution and its morphology. Figure 7 shows how the response of the system for a same amplitude of initial perturbation having non-dimensional value of, $A \sim 0.08$ varies under two different ducting conditions. The left hand side of the figure shows the bore evolution for a narrow duct (Case-1) having a FWHM value of ~1 while that on the right is a wider duct having a value of ~2 (Case-5). Clear distinction in the bore characteristics such as the time of formation of the first peak, steepening of the wavefront, number of trailing waves and the dissipation of the bore can be readily seen between the two simulation runs. Both the systems are initialized with a perturbation of same amplitude at $T = 0$ s. While Case-1 results in the formation of a peak at $T = 50$ s, the response of the Case-5 is different in that it is still exhibiting a systematic steepening at the same time. Evidently structure of the duct also plays a role in the peak amplitude attained by the bore as seen in Figure 7 where Case-1 attains a lower peak value (~0.06) than Case-5 (wide duct) whose peak value is ~0.12 which is 1.5 times the initial amplitude. The dependence of the degree of bore undularity on the duct depth has been theoretically explained by Dewan and Picard (1998) and reported in observations by S. M. Smith et al. (2003) and Mondal et al. (2021). It is also interesting to note the influence of the duct width has on the bore dissipation. It is seen very clearly in Figure 7
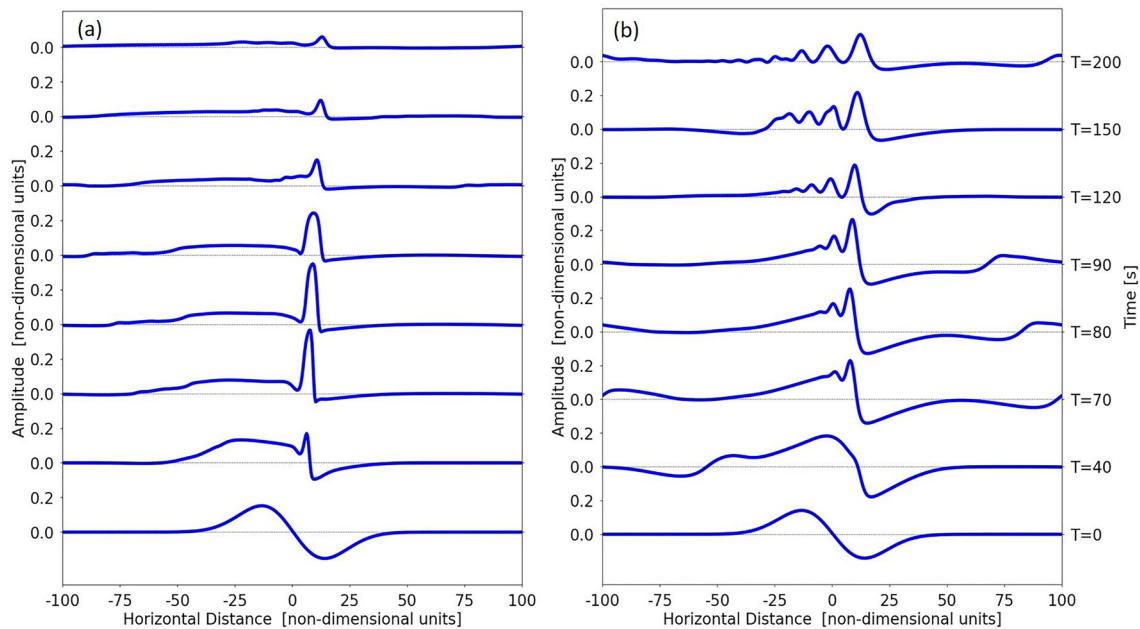
Figure 8. As in Figure 7 but with initial amplitude, $A \sim 0.16$ to see the effect of varying initial amplitude on bore evolution (a) Solitary wave response for Case-1 (b) Undular bore response for Case-5.

that Case-1 experiences a faster dissipation of the bore ($T \sim 200$ s) whereas at the same time the bore is fully evolved for Case-5. Thus, we suspect that for a narrow duct the energy loss to the outside of the duct is more than that for a wider duct.

Since the wave steepening is a non-linear effect, we increased the amplitude of the initial perturbation by a factor of 2 to a non-dimensional value of $A \sim 0.16$ in order to increase the effect of non-linearity and its effect on bore evolution. Figure 8 displays the temporal evolution of the potential temperature field when the simulation was initialized with the above mentioned amplitude for a Case-1 and Case-5. It can be seen that when the initial perturbation amplitude is the same, the system yields a solitary wave response (one dominant peak) for the Case-1 (narrow duct) while undular bore structure for Case-5 (wider duct). The sharp peak feature of the solitary wave is apparent at time $T = 40$ s which eventually unstable attaining a peak amplitude that is at least 2.5 times the initial amplitude of perturbation. A flow is thought to be unstable if any disturbance will have noticeable effects on the state of the system, which could cause it to grow in amplitude rapidly (Drazin & Reid, 2004). This rapid response of Case-1 to an initial perturbation resulting in a soliton-like structure is completely different from the response obtained when the duct is wide (Case-5). As can be seen on the right side of Figure 8 in Case-5, the system yields a response that resembles non-linear wave steepening of the initial perturbation resulting in a bore-like structure where trailing undulations are evident. The solitary wave structure in the Case-1 also loses its energy rather faster compared to the undular bore structure in Case-5.

A more comprehensive discussion on the effects of ducting width and the initial perturbation on the bore evolution is given in Section 4.

4. Discussion

Even though plenty of literature exists on observations of the mesospheric bores using the all-sky imagers, and satellite measurements (Bageston et al., 2011; Fechine et al., 2005, 2009; Narayanan et al., 2009; Nielsen et al., 2006; She et al., 2004; S. M. Smith et al., 2003, 2005; Yue et al., 2010), the formation mechanisms of bores in the MLT region are still not well understood. In the present investigation, we observed an upward propagating gravity wave evolving into a bore in the upper mesosphere. In addition, using DNS simulations we have reproduced many of the features of the observed bore event and further explored the suitable background conditions and controlling factors for the generation of the bores in general.

In the present study, we have investigated to what extent the thermal duct alone could reproduce some of the observed bore features and to this effect the background ducting condition used in this study is a more generic representation of the thermal duct. We are simulating the bore dynamics at one particular altitude where the thermal duct is situated, and in addition, we also assume that the perturbation which is given as an initial condition is a ducted gravity wave at a particular altitude that may evolve as a bore under a given background condition. Since our intent was not compare the simulation results with those of the observations but rather reproduce the features of the observed bore using idealized simulations, this assumption of simulating the bore evolution and propagation at one particular altitude seemed valid. To simulate an upward propagating gravity wave encountering an inversion layer and the complexities involving multiple ducts a more comprehensive model may be required which is not the focus of the current work. Furthermore in the current work, we have only explored the effects of changing the background stability profile and its consequence on the bore evolution. Currently, we are working to include the effects of background wind variability on the formation of the duct for the generation of bores.

Initial DNS results from Figure 6 show that the many of the characteristics of the observed undular bore can be reproduced by using an idealized 2D Boussinesq model with a thermal duct under a constant background wind condition (no background wind shear). By initializing the simulation with a sinusoidal waveform, the nonlinear wave-steepening resembling a hydraulic jump mechanism is reproduced which looks very similar to the observations ($T = 50$ s in Figure 6b). This hydraulic jump phenomena is frequently observed in open channel flows where step-like wave or undulation of water moves upstream against water flowing downstream leading to the formation of tidal bores (Rayleigh, 1908). The initial sinusoidal waveform had a non-dimensional horizontal wavelength of 60 which is much smaller than the simulation horizontal domain (a non-dimensional value of 200). This is different from the previous modeling works of Seyler (2005) and Laughman et al. (2009) who had considered a horizontal wavelength of the initial perturbation to be the size of the entire domain. We believe that with the initial conditions considered here, we are realistically simulating the formation of undular bore. There is a good agreement between the airglow observations and simulations regarding the formation of a sharp peak following the wave-steepening and the subsequent appearance of trailing waves (3 in total). This provides evidence that our simulations do indeed capture the morphology of the bore evolution in a good way. In contrast, the simulations done by Seyler (2005) did not consider the effect of dissipation when using potential temperature as a passive scalar on the bore evolution. That led to large number of trailing undulations (>8) being formed while typical airglow observations of mesospheric undular bores report 4–5 trailing waves. The rate of addition of the trailing waves is an indicator of the dissipation rate of the bore (Dewan & Picard, 1998). In the present case, the waves are added at a rate of around 2 waves per hour which is close to the value reported by S. M. Smith et al. (2003).

In order to further compare the results from observation and simulation, we scale our DNS results back to the physical space and time units. We set the length scale to be $\sim$1.5 km which is approximately the half-width of thermal duct near the altitude of O(^{1}S) emission layer from the observations and then the effective horizontal wavelength of the longest undulation in Figure 6b is $\sim$20 km (determined approximately 3/4 of way through simulation) which agrees relatively well with the wavelength of the observed bore (Figure 6a, $\sim$25 km). Seyler (2005) also reported similar values of horizontal wavelength for the longest undulation. Taking into account the maximum buoyancy frequency of $\sim$0.032 s^{-1} from Figure 4, the time taken for the simulated bore to dissipate is around 135 min which is close to the lifetime of the undular bore reported here ($\sim$120 min, Figures 2 and 6). As far as the present study is concerned, the obtained results from the DNS even only under a thermal duct and constant background wind show a good agreement with the observations regarding the bore morphology. However, the horizontal winds show a notable change in their values during the time of bore observation (see Figure 7). From the observations, it seems that the resultant background wind may have also provided a conducive background in the form of Doppler duct for bore propagation near the (O^{1}S) peak emission altitude. Fechine et al. (2009) reported the importance of the Doppler duct in the formation of undular mesospheric bores although in their study they also found the presence of a temperature inversion layer during the bore observation. Therefore, one of our future goals is to quantify the effects of the background wind shear, in addition to the thermal duct effects, on the bore evolution and propagation using DNS.

Figure 9 shows the effects of different thermal ducting conditions and the initial perturbations on the bore formation time, the nonlinearity of bore evolution and time taken for the bore to dissipate. The upper left plot (Figure 9a) shows the role of duct width on the formation time of the bore under different amplitudes of the initial perturbation. The bore formation time is the time for the emergence of the first dominant peak. It can be seen in Figure 9a that the time taken for the bore to form increases as the width of the duct increases, for a constant initial
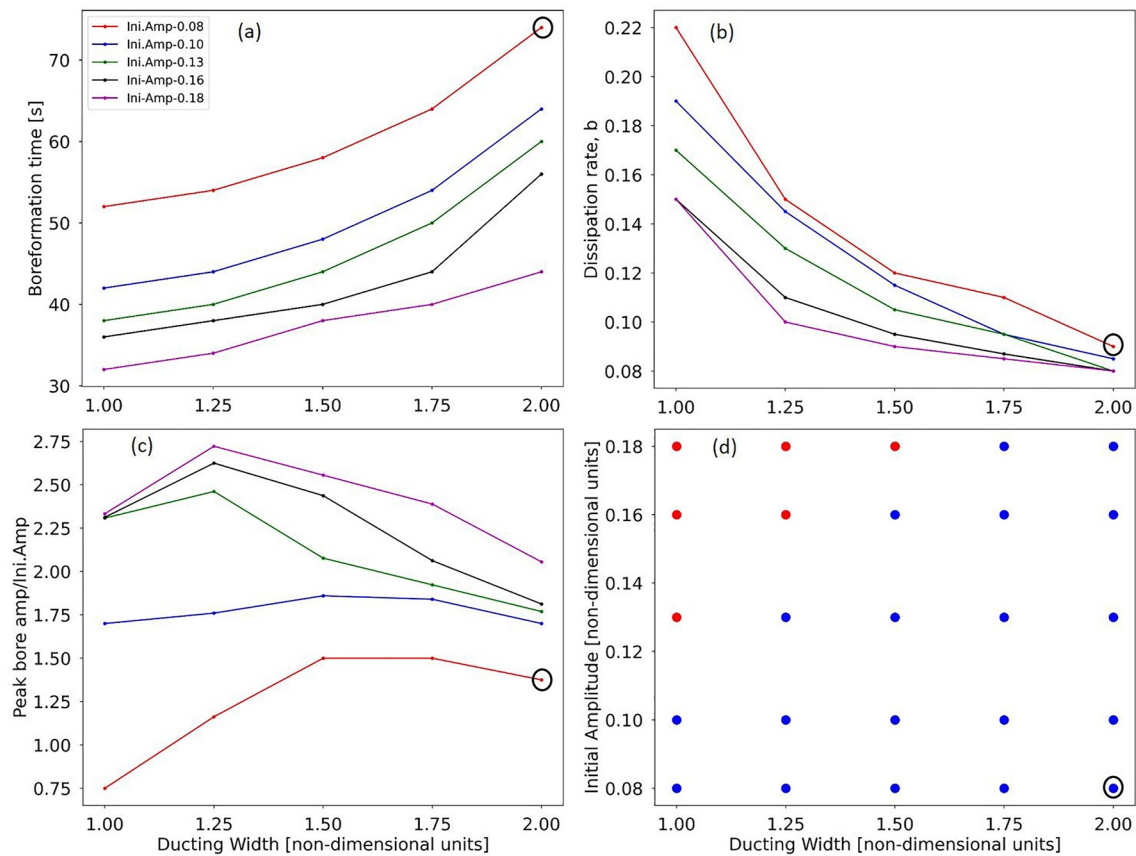
Figure 9. Plots showing the effects of varying ducting widths and initial perturbation on (a) Formation time of the bore, (b) Dissipation rate of bore given by ae^{-bt}, where $a = 0.8$, (c) The peak amplitude of the bore (non-linearity), and (d) Solitary wave-like response (red dots) and undular-bore like response (blue dots). The black circles in the plots indicate the parameters of the simulation case considered to compare our undular bore observation.

amplitude perturbation. Conversely for a constant duct width, the bore formations time decreases as the initial amplitude perturbation is increased. Laughman et al. (2009) reported that by narrowing the width of the duct, the resulting behavior of the bore was more nonlinear and the response of the system was more rapid in forming a bore. Summarizing the above in a more concise way, for the simulation settings considered here, the following two relations are drawn between the duct width, initial amplitude and bore formation time,

- If the initial amplitude is constant then the bore formation time is proportional to the width of the duct.
- If duct width is constant then the bore formation time is inversely proportional to the initial amplitude of perturbation.

Figure 9b shows the effect of the duct width on the rate of dissipation of the bore for different initial amplitudes. From the simulations, the amplitude of the bore as a function of time was obtained and an iterative process was implemented to determine the curve that best fit this data for each case. For a constant initial amplitude of perturbation, we can see that the bore takes longer time to dissipate as the width of the duct increases. This means that in a narrow duct the bore dissipates its energy faster to the surrounding than in a wide duct. Reduction in the stability away from the duct could be a reason for this. This behavior is consistent for all the simulated values of initial perturbation. Connecting the dissipation rate to the bore formation time we can conclude that for a constant amplitude, as the width of the duct increases the bore takes longer to form and takes longer to dissipate. This was also apparent from Figure 8 where for a given high amplitude initial perturbation, the response of Case-1 is more rapid resulting in the quicker evolution of the peak compared to Case-5 and subsequently followed by faster dissipation in the Case-1 (narrow duct). Consequently, if the amplitude of initial perturbation is high, then the time for dissipation is also longer, for a duct of constant width as is shown in Figure 9b. This makes sense since, physically if the initial amplitude of perturbation of a system is high then it has more energy and therefore takes longer to

fully dissipate, in the absence of external forces and when energy is removed only by viscosity. Summarizing this result, we can draw the following relations between the dissipation rate, the amplitude and the duct width,

- For a constant amplitude of initial perturbation, as width of the duct increases the dissipation rate decreases.
- For a constant duct width, lower the amplitude of initial perturbation, higher is the dissipation rate.

The influence of duct thickness on the non-linearity of the bore evolution is shown in Figure 9c. The amplitude ratio is defined as ratio of the peak amplitude that the bore reaches to the initial amplitude of perturbation. It can be seen that there is a clear distinction between the response of low and high initial amplitude perturbations. For higher initial amplitudes, a maximum peak bore amplitude was obtained for Case-2. Any further increase in the duct width resulted in a decrease in the peak bore amplitude. Also note that for the initial amplitude $A \sim 0.10$, the peak amplitude is more or less constant across different duct widths. This leads us to postulate this amplitude may be considered as a critical amplitude which is not affected by changes in the background ducting conditions for the simulation settings considered. In Figure 9d is shown the conditions for the formation of undular bore and solitary wave. For the background conditions considered in the simulations, only the two low initial perturbation values ($A \sim 0.08, 0.10$) resulted in the formation of bore for all the duct widths simulated, whereas for high initial amplitudes, depending on the duct width, the response of the system was either a solitary wave or a bore. Coincidentally, the solitary wave responses were obtained for the cases with higher initial amplitudes and narrow ducts. This could mean that the solitary wave response may depend on the strength of the nonlinearity of the system. Laughman et al. (2009) also reported soliton-like responses for simulations under the conditions of high initial amplitude of perturbation and narrow duct which in their case was defined by a cosine profile in a deep domain where the vertical extent of the domain was at least 10 times larger than the one considered here. The measure of nonlinearity of undular bores is given by the parameter $a\lambda^2/h^3$, where a is the elevation of the perturbation above the free surface, λ is the wavelength and h is the thickness of the duct (Dewan & Picard, 1998; Lighthill, 1978). This indicates that the degree of the nonlinearity of the system depends inversely on the duct thickness. Hence this could offer a explanation why strong nonlinear responses were obtained when the duct width was reduced indicating that the gradient of the stability profile may play a role in supporting this behavior (Laughman et al., 2009; Lighthill, 1978).

It is well known that inversion layers are a common occurrence in the mesosphere (Meriwether & Gerrard, 2004). But not all inversion layers lead to bore formation. Our results indicate that under different ducting and initial perturbation conditions, one can expect variety of responses (see Section 4). Many of these responses like the short period solitary waves which could not have been observed due to observational limitations. The results presented here have provided evidence of the possible range of nonlinear response in different complex background environments. In doing so, we have only scratched the surface in understanding the dynamics of mesospheric bores. Many overarching questions like the plausible generation mechanisms of mesospheric bores due to vertically propagating GWs (Chimonas & Hines, 1986), critical layer interaction (Dewan & Picard, 2001) and local forcing accompanying GW breaking (Fritts et al., 2020) are still unexplored by modeling. Moreover, a recent observation of extreme vertical drafts (± 50 ms^{-1}) in the mesosphere showing characteristics that resemble a soliton in varicose mode (Chau et al., 2021) indicates that further modeling efforts are needed to better understand and characterize the potential sources of kilometer-scale instabilities. Furthermore, it is clear from the dispersion relation that large-scale winds can also play a crucial role in GW ducting and bore formation (S. M. Smith et al., 2017). These result in potential Doppler-thermal ducts which are more likely to be found in MLT. As a future work, the contribution of a background wind shear and more realistic initial conditions will be inspected with regard to the generation and evolution of bores.

5. Conclusion

We have presented the observation of a bright mesospheric bore event that occurred over northern Germany during the night of 16 March 2021. The observed event is identified as an undular mesospheric bore type with trailing undulations. The analysis of SABER data suggest the presence of a temperature inversion above 95 km could have served as a duct for the bore propagation. Further analysis of the brightness intensity of different emission layers suggest that this event could have been caused due to the nonlinear interaction of upward propagating GWs with the inversion layer. The nonlinear steepening of the wavefront, the subsequent formation of at least three trailing waves and the ensuing dissipation were clearly captured by the imager. This bore observation is

also characterized by a rapid dissipation with the time duration for dissipation being less than 20 min. This rapid dissipation of the bore could have been a result of leakage of energy from the duct.

Furthermore, to understand the controlling factors behind the bore formation, we ran a series of Direct Numerical Simulations of a 2D model based on Boussinesq approximation by including the diffusion term. Our results demonstrated that the idealized 2D simulations can reproduce the bore-like shape of the observed event in an extraordinarily good way by initializing a small-scale perturbation under thermal ducting condition. In addition to that, the horizontal wavelength between the first peak and the trailing wave, and number of trailing waves are also reproduced in the simulations. We also looked into how the varying duct thickness and initial perturbation affect bore parameters like, formation and dissipation time of the bore, peak bore amplitude and the number of trailing undulations formed. From this analysis, we have the following conclusions: (a) For a constant initial perturbation, the bore forms faster when the duct is narrow. A narrow duct also has fewer number of trailing undulations. In contrast, in a wider duct the bore takes longer time to form as well as to dissipate and has more number of trailing undulations; (b) for a constant duct thickness, if the amplitude of the initial perturbation is large, then bore forms faster, takes more time to dissipate and has more number of trailing undulations. A solitary wave response is obtained only for a narrow duct with high initial amplitude perturbation. Mesospheric bores may play an important role in understanding the dynamics of the MLT, particularly regarding the transport of energy and momentum and as such a lot could be learned from investigating their formation and evolution.

Data Availability Statement

The data used to generate the figures presented in this manuscript can be found at https://doi.org/10.22000/809. The airglow imager data used in this paper were obtained from http://sirius.bu.edu/data/. The temperature profiles from TIMED SABER used here was acquired from http://saber.gats-inc.com/coin.php.

References

Asokan, H. C., Chau, J. L., Marino, R., Vierinen, J., Vargas, F., Urco, J. M., et al. (2022). Frequency spectra of horizontal winds in the mesosphere and lower thermosphere region from multistatic specular meteor radar observations during the SIMONe 2018 campaign. *Earth Planets and Space*, *74*(1), 69. https://doi.org/10.1186/s40623-022-01620-7

Bageston, J. V., Wrasse, C. M., Batista, P. P., Hibbins, R. E., Fritts, D. C., Gobbi, D., & Andrioli, V. F. (2011). Observation of a mesospheric front in a thermal-Doppler duct over king George Island, Antarctica. *Atmospheric Chemistry and Physics*, *11*(23), 12137–12147. https://doi.org/10.5194/acp-11-12137-2011

Brown, L. B., Gerrard, A. J., Meriwether, J. W., & Makela, J. J. (2004). All-sky imaging observations of mesospheric fronts in oi 557.7 nm and broadband oh airglow emissions: Analysis of frontal structure, atmospheric background conditions, and potential sourcing mechanisms. *Journal of Geophysical Research D: Atmospheres*, *109*(D19), D19104. https://doi.org/10.1029/2003JD004223

Burns, K. J., Vasil, G. M., Oishi, J. S., Lecoanet, D., & Brown, B. P. (2020). Dedalus: A flexible framework for numerical simulations with spectral methods. *Physical Review Research*, *2*, 023068. https://doi.org/10.1103/PhysRevResearch.2.023068

Chau, J. L., Marino, R., Feraco, F., Urco, J. M., Baumgarten, G., Lübken, F., et al. (2021). Radar observation of extreme vertical drafts in the polar summer mesosphere. *Geophysical Research Letters*, *48*(16), e2021GL094918. https://doi.org/10.1029/2021GL094918

Chau, J. L., Urco, J. M., Avsarkisov, V., Vierinen, J. P., Latteck, R., Hall, C. M., & Tsutsumi, M. (2020). Four-dimensional quantification of Kelvin-Helmholtz instabilities in the polar summer mesosphere using volumetric radar imaging. *Geophysical Research Letters*, *47*(1), e2019GL086081. https://doi.org/10.1029/2019GL086081

Chau, J. L., Urco, J. M., Vierinen, J. P., Volz, R. A., Clahsen, M., Pfeffer, N., & Trautner, J. (2019). Novel specular meteor radar systems using coherent MIMO techniques to study the mesosphere and lower thermosphere. *Atmospheric Measurement Techniques*, *12*(4), 2113–2127. https://doi.org/10.5194/amt-12-2113-2019

Chimonas, G., & Hines, C. O. (1986). Doppler ducting of atmospheric gravity waves. *Journal of Geophysical Research*, *91*(D1), 1219. https://doi.org/10.1029/JD091iD01p01219

Clarke, R. H. (1972). The morning glory: An atmospheric hydraulic jump. *Journal of Applied Meteorology*, *11*(2), 304–311. https://doi.org/10.1175/1520-0450(1972)011<0304:TMGAAH>2.0.CO;2

Conte, J. F., Chau, J. L., Liu, A., Qiao, Z., Fritts, D. C., Hormaechea, J. L., et al. (2022). Comparison of MLT momentum fluxes over the Andes at four different latitudinal sectors using multistatic radar configurations. *Journal of Geophysical Research: Atmospheres*, *127*(4), e2021JD035982. https://doi.org/10.1029/2021JD035982

Dalin, P., Connors, M., Schofield, I., Dubietis, A., Pertsev, N., Perminov, V., et al. (2013). First common volume ground-based and space measurements of the mesospheric front in noctilucent clouds. *Geophysical Research Letters*, *40*(24), 6399–6404. https://doi.org/10.1002/2013gl058553

Dawkins, E. C. M., Feofilov, A., Rezac, L., Kutepov, A. A., Janches, D., Höffner, J., et al. (2018). Validation of saber v2.0 operational temperature data with ground-based lidars in the mesosphere-lower thermosphere region (75–105 km). *Journal of Geophysical Research: Atmospheres*, *123*(17), 9916–9934. https://doi.org/10.1029/2018JD028742

Dewan, E. M., & Picard, R. H. (1998). Mesospheric bores. *Journal of Geophysical Research*, *103*(D6), 6295–6305. https://doi.org/10.1029/97JD02498

Dewan, E. M., & Picard, R. H. (2001). On the origin of mesospheric bores. *Journal of Geophysical Research*, *106*(D3), 2921–2927. https://doi.org/10.1029/2000JD900697

Drazin, P. G., & Reid, W. H. (2004). *Hydrodynamic stability* (2nd ed.). Cambridge University Press. https://doi.org/10.1017/CBO9780511616938

Dubietis, A., Dalin, P., Balčiūnas, R., Černis, K., Pertsev, N., Sukhodoev, V., et al. (2011). Noctilucent clouds: Modern ground-based photographic observations by a digital camera network. *Applied Optics*, *50*(28), F72. https://doi.org/10.1364/ao.50.000f72

Fechine, J., Medeiros, A. F., Buriti, R. A., Takahashi, H., & Gobbi, D. (2005). Mesospheric bore events in the equatorial middle atmosphere. *Journal of Atmospheric and Solar-Terrestrial Physics*, *67*(17–18), 1774–1778. https://doi.org/10.1016/j.jastp.2005.04.006

Fechine, J., Wrasse, C. M., Takahashi, H., Medeiros, A. F., Batista, P. P., Clemesha, B. R., et al. (2009). First observation of an undular mesospheric bore in a Doppler duct. *Annales Geophysicae*, *27*(4), 1399–1406. https://doi.org/10.5194/angeo-27-1399-2009

Fritts, D. C., Kaifler, N., Kaifler, B., Geach, C., Kjellstrand, C. B., Williams, B. P., et al. (2020). Mesospheric bore evolution and instability dynamics observed in PMC turbo imaging and Rayleigh lidar profiling over northeastern Canada on 13 July 2018. *Journal of Geophysical Research: Atmospheres*, *125*(14), e2019JD032037. https://doi.org/10.1029/2019JD032037

Garcia, F. J., Kelley, M. C., Makela, J. J., & Huang, C.-S. (2000). Airglow observations of mesoscale low-velocity traveling ionospheric disturbances at midlatitudes. *Journal of Geophysical Research*, *105*(A8), 18407–18415. https://doi.org/10.1029/1999JA000305

García-Comas, M., López-Puertas, M., Marshall, B. T., Wintersteiner, P. P., Funke, B., Bermejo-Pantaleón, D., et al. (2008). Errors in sounding of the atmosphere using broadband emission radiometry (saber) kinetic temperature caused by non-local-thermodynamic-equilibrium model parameters. *Journal of Geophysical Research*, *113*(D24), D24106. https://doi.org/10.1029/2008JD010105

Hecht, J. H., Walterscheid, R. L., & Vincent, R. A. (2001). Airglow observations of dynamical (wind shear-induced) instabilities over Adelaide, Australia, associated with atmospheric gravity waves. *Journal of Geophysical Research*, *106*(D22), 28189–28197. https://doi.org/10.1029/2001JD000419

Hines, C. O. (1960). Internal atmospheric gravity waves at ionospheric heights. *CaJPh*, *38*(11), 1441–1481. https://doi.org/10.1139/P60-150

Hozumi, Y., Saito, A., Sakanoi, T., Yamazaki, A., & Hosokawa, K. (2018). Mesospheric bores at southern midlatitudes observed by ISS-IMAP/VISI: A first report of an undulating wave front. *Atmospheric Chemistry and Physics*, *18*(22), 16399–16407. https://doi.org/10.5194/acp-18-16399-2018

Hozumi, Y., Saito, A., Sakanoi, T., Yamazaki, A., Hosokawa, K., & Nakamura, T. (2019). Geographical and seasonal variability of mesospheric bores observed from the international space station. *Journal of Geophysical Research: Space Physics*, *124*(5), 3775–3785. https://doi.org/10.1029/2019JA026635

Isler, J. R., Taylor, M. J., & Fritts, D. C. (1997). Observational evidence of wave ducting and evanescence in the mesosphere. *Journal of Geophysical Research*, *102*(D22), 26301–26313. https://doi.org/10.1029/97jd01783

Laughman, B., Fritts, D. C., & Werne, J. (2009). Numerical simulation of bore generation and morphology in thermal and Doppler ducts. *Annales Geophysicae*, *27*(2), 511–523. https://doi.org/10.5194/angeo-27-511-2009

Li, F., Swenson, G. R., Liu, A. Z., Taylor, M., & Zhao, Y. (2007). Investigation of a "wall" wave event. *Journal of Geophysical Research*, *112*(D4), D04104. https://doi.org/10.1029/2006JD007213

Lighthill, M. J. (1978). *Waves in fluids*. Cambridge University Press. https://doi.org/10.1002/cpa.3160200204

Martinis, C., Baumgardner, J., Wroten, J., & Mendillo, M. (2018). All-sky-imaging capabilities for ionospheric space weather research using geomagnetic conjugate point observing sites. *Advances in Space Research*, *61*(7), 1636–1651. https://doi.org/10.1016/j.asr.2017.07.021

Meriwether, J., & Gerrard, A. (2004). Mesosphere inversion layers and stratosphere temperature enhancements. *Reviews of Geophysics*, *42*(3), RG3003. https://doi.org/10.1029/2003RG000133

Mondal, S., Sivakandan, M., Sarkhel, S., Krishna, M. V. S., Mlynczak, M. G., Russell, J. M., & Bharti, G. (2021). A case study of a thermally ducted undular mesospheric bore accompanied by ripples over the western Himalayan region. *Advances in Space Research*, *68*(3), 1425–1440. https://doi.org/10.1016/j.asr.2021.03.026

Nappo, C. J. (2013). *An introduction to atmospheric gravity waves* (2nd ed. ed.). Elsevier.

Narayanan, V. L., Gurubaran, S., & Emperumal, K. (2009). A case study of a mesospheric bore event observed with an all-sky airglow imager at Tirunelveli (8.7°N). *Journal of Geophysical Research*, *114*(D8), D08114. https://doi.org/10.1029/2008JD010602

Nielsen, K., Taylor, M. J., Stockwell, R. G., & Jarvis, M. J. (2006). An unusual mesospheric bore event observed at high latitudes over Antarctica. *Geophysical Research Letters*, *33*(7), L07803. https://doi.org/10.1029/2005GL025649

Peterson, A. W., & Adams, G. W. (1983). Oh airglow phenomena during the 5–6 July 1982 total lunar eclipse. *Applied Optics*, *22*(17), 2682. https://doi.org/10.1364/ao.22.002682

Poblet, F. L., Chau, J. L., Conte, J. F., Avsarkisov, V., Vierinen, J., & Asokan, H. C. (2022). Horizontal wavenumber spectra of vertical vorticity and horizontal divergence of mesoscale dynamics in the mesosphere and lower thermosphere using multistatic specular meteor radar observations. *Earth and Space Science*, *9*(9), e2021EA002201. https://doi.org/10.1029/2021ea002201

Rayleigh (1908). Note on tidal bores. *Proceedings of the Royal Society of London—Series A: Containing Papers of a Mathematical and Physical Character*, *81*. https://doi.org/10.1098/rspa.1908.0102

Sarkhel, S., Stober, G., Chau, J. L., Smith, S. M., Jacobi, C., Mondal, S., et al. (2022). A case study of a ducted gravity wave event over northern Germany using simultaneous airglow imaging and wind-field observations. *Annales Geophysicae*, *40*(2), 179–190. https://doi.org/10.5194/angeo-40-179-2022

Seyler, C. E. (2005). Internal waves and undular bores in mesospheric inversion layers. *Journal of Geophysical Research D: Atmospheres*, *110*(D9), D09S05. https://doi.org/10.1029/2004JD004685

She, C. Y., Li, T., Williams, B. P., Yuan, T., & Picard, R. H. (2004). Concurrent oh imager and sodium temperature/wind lidar observation of a mesopause region undular bore event over fort Collins/Platteville, Colorado. *Journal of Geophysical Research D: Atmospheres*, *109*(D22), D22107. https://doi.org/10.1029/2004JD004742

Sivakandan, M., Chakrabarty, D., Ramkumar, T. K., Guharay, A., Taori, A., & Parihar, N. (2019). Evidence for deep ingression of the midlatitude MSTID into as low as 3.5° magnetic latitude. *Journal of Geophysical Research: Space Physics*, *124*(1), 749–764. https://doi.org/10.1029/2018JA026103

Smith, R. K. (1988). Travelling waves and bores in the lower atmosphere: The 'morning glory' and related phenomena. *Earth-Science Reviews*, *25*(4), 267–290. https://doi.org/10.1016/0012-8252(88)90069-4

Smith, S. M., Friedman, J., Raizada, S., Tepley, C., Baumgardner, J., & Mendillo, M. (2005). Evidence of mesospheric bore formation from a breaking gravity wave event: Simultaneous imaging and lidar measurements. *Journal of Atmospheric and Solar-Terrestrial Physics*, *67*(4), 345–356. https://doi.org/10.1016/j.jastp.2004.11.008

Smith, S. M., Stober, G., Jacobi, C., Chau, J. L., Gerding, M., Mlynczak, M. G., et al. (2017). Characterization of a double mesospheric bore over Europe. *Journal of Geophysical Research: Space Physics*, *122*(9), 9738–9750. https://doi.org/10.1002/2017JA024225

Smith, S. M., Taylor, M. J., Swenson, G. R., She, C.-Y., Hocking, W., Baumgardner, J., & Mendillo, M. (2003). A multidiagnostic investigation of the mesospheric bore phenomenon. *Journal of Geophysical Research*, *108*(A2), 1083. https://doi.org/10.1029/2002ja009500

Taylor, M. J., & Hapgood, M. A. (1990). On the origin of ripple-type wave structure in the OH nightglow emission. *Planetary and Space Science*, *38*(11), 1421–1430. https://doi.org/10.1016/0032-0633(90)90117-9

Taylor, M. J., Pendleton, W. R., Jr., Clark, S., Takahashi, H., Gobbi, D., & Goldberg, R. A. (1997). Image measurements of short-period gravity waves at equatorial latitudes. *Journal of Geophysical Research*, *102*(D22), 26283–26299. https://doi.org/10.1029/96JD03515

Taylor, M. J., Turnbull, D. N., & Lowe, R. P. (1995). Spectrometric and imaging measurements of a spectacular gravity wave event observed during the aloha-93 campaign. *Geophysical Research Letters*, *22*(20), 2849–2852. https://doi.org/10.1029/95GL02948

Walterscheid, R. L., Hecht, J. H., Vincent, R. A., Reid, I. M., Woithe, J., & Hickey, M. P. (1999). Analysis and interpretation of airglow and radar observations of quasi-monochromatic gravity waves in the upper mesosphere and lower thermosphere over Adelaide, Australia (35°S, 138°E). *Journal of Atmospheric and Solar-Terrestrial Physics*, *61*(6), 461–478. https://doi.org/10.1016/S1364-6826(99)00002-4

Yue, J., She, C.-Y., Nakamura, T., Harrell, S., & Yuan, T. (2010). Mesospheric bore formation from large-scale gravity wave perturbations observed by collocated all-sky oh imager and sodium lidar. *Journal of Atmospheric and Solar-Terrestrial Physics*, *72*(1), 7–18. https://doi.org/10.1016/j.jastp.2009.10.002